C. R. Physique 11 (2010) 216–225

Contents lists available at ScienceDirect

Comptes Rendus Physique

www.sciencedirect.com

Computational metallurgy and changes of scale / Métallurgie numérique et changements d'échelle

Modeling of solidification: Grain structures and segregations in metallic alloys

Modélisation de la solidification : Structures de grains et ségrégations des alliages métalliques

Charles-André Gandin

MINES-ParisTech, CEMEF UMR CNRS 7635, 06904 Sophia Antipolis cedex, France

ARTICLE INFO

Article history:
Available online 30 August 2010

Keywords:
Solidification
Modeling
Structure
Segregation
Metallic alloys

Mots-clés :
Solidification
Modélisation
Structure
Ségrégation
Alliages métalliques

ABSTRACT

Modeling of solidification for applications to processing of metallic alloys is often restricted to microsegregation (segregation of chemical species taking place between dendrite arms) with the objective to predict the phase fractions in the as-cast state. This approach can be entirely conducted based on thermodynamic equilibrium. It can also include limited diffusion of the chemical species, in which case length scales such as the dendrite arm spacing or the grain size are required. Another approach is to model the kinetics and shape of a solid–liquid interface. While this approach gives a direct and complete description of the structure and segregation, it is limited to extremely small domains due to the heavy computational resources required, with no hope to reach applications up to the casting scale. New developments over the last decade have permitted to combine the description of microsegregation with a direct modeling approach of grain structure and macrosegregation (deviation of the alloy composition within the cast part). Such developments are illustrated, together with perspectives expected to take place in the near future.

RÉSUMÉ

La modélisation de la solidification pour applications à la mise en forme des alliages métalliques est encore trop souvent réduite à la microségrégation (ségrégation des espèces chimiques prenant place entre les bras des dendrites) avec l'objectif de prédire les fractions de phase dans l'état brut de coulée. Cette approche peut être entièrement conduite en se basant sur des équilibres thermodynamiques. Elle peut aussi inclure des considérations sur la diffusion, auquel cas des échelles de longueurs telles que l'espacement interdendritique ou la taille de grain sont requis. L'autre tendance est de modéliser directement la propagation de l'interface solide–liquide. Bien que cette approche donne une description directe et complète de la structure et de la ségrégation, elle est limitée à des domaines extrêmement petits compte tenu des ressources calculatoires élevées nécessaires, avec peu d'espoir d'atteindre des applications à l'échelle de la coulée dans un futur proche. De nouveaux développements au cours des dix dernières années ont permis de combiner la description de la microségrégation avec une modélisation directe de la structure de grains et de la macroségrégation (variation de la composition de l'alliage au sein du produit

E-mail address: charles-andre.gandin@mines-paristech.fr.

1631-0705/$ – see front matter
doi:10.1016/j.crhy.2010.07.010

coulée). De tels développements sont illustrés, avec les perspectives d'évolution attendues dans un futur proche.

1. Introduction

Modeling of solidification has been the topic of several reviews for the last two decades [1–7]. While the first review was effectively centered on modeling of structure formation during casting, the following exercises were more specialized on modeling of microsegregation [2], dendritic and peritectic growths [3,4], macrosegregation [5], columnar-to-equiaxed transition [6], or texture formation in materials processing [7]. Other reviews recently considered solidification microstructure, with limited interest on the macroscopic scale [8]. The present article is dedicated to the latter issue, i.e. modeling of the formation of the solidification structure with the goal to reach a description at the scale of the casting.

Fig. 1 schematizes a domain undergoing solidification. The metallic alloy is chosen to solidify with a primary dendritic structure. This is actually the case for most alloys of industrial relevance. Several modeling approaches exist, the output of which is made available in Figs. 1(a)–1(c) in terms of structural parameters. *Direct microscopic modeling* provides with a description of the development of the solid–liquid interface, including its destabilization due to the segregation of solute elements at the interface to produce the dendritic microstructure shown in Fig. 1(a). It is the most precise approach with respect to the spatial distribution of phases and chemical species. The methods to reach such descriptions are several, including front tracking [9], phase field [10,11], volume averaging with interface tracking [12,13] or level set [14,15]. While the dendritic structure is fully and directly accessible, this approach suffers from requiring very heavy computational resources. For this reason, coupling with heat flow is rarely considered [16] and dedicated numerical approximate methods had to be proposed in order to reach some practical applications [17], especially when the objective is linked to three-dimensional predictions. Despite the progress of computers and methods over the last decades, as well as the continuing improvements expected in computer science, there is no hope today that such direct microscopic modeling methods could be applied to real cast parts. *Direct microscopic modeling* will thus remain limited to comparison with indirect microscopic models. They could be useful to give improved modeling of the smallest length scales of the structure such as the dendrite tip radius or the dendrite arm spacing, that are necessary for larger scale modeling. Also note that the grain density, denoted n in Fig. 1(a), usually remains an input parameter to be provided to this approach.

Indirect macroscopic modeling of structures and segregations is based on averaging methods to integrate the conservation equations [5]. A coupled solution for heat and mass transfers is given, with distinction between the total mass and the mass of solute elements. The topological distribution of the phases and species is not directly simulated. This is illustrated in Fig. 1(c) where no structure is sketched. Instead, the microstructure is approximated by variables representing its length scales such as the dendrite tip radius, r, the dendrite arm spacing, λ_2, the radius of the grains, R, and the grain density, n [18–27]. The determination of these length scales requires using additional indirect microscopic models, input mentioned by the text added in Fig. 1(c). The main advantage of introducing approximate descriptions of the microstructure length scales is the possibility to deal with large castings while not describing the detailed development of the solid–liquid interface leading to the final structure. This approach is the most advanced for applications to ingots and casting [28–39]. It can be seen as

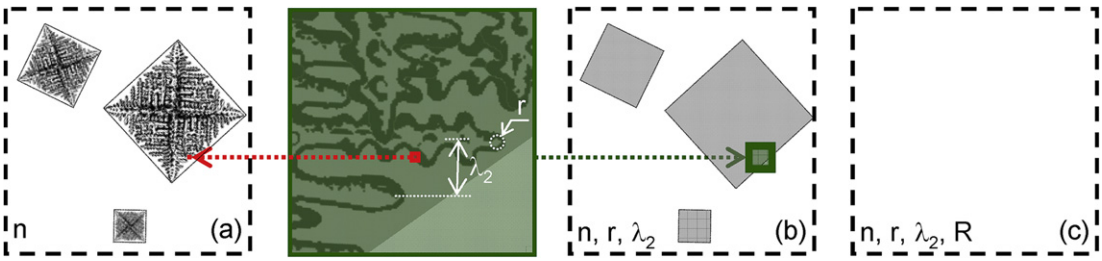

Fig. 1. Schematics of (dashed black and white contours) a representative domain for the study of the dendritic structure and its associated chemical segregation formed during solidification and (plain colored contours) typical integration volumes for the conservation equations for (a) direct microscopic modeling, (b) direct macroscopic modeling and (c) indirect macroscopic modeling. The illustration inserted between (a) and (b) presents a better view of the integration volumes and the definition of the dendrite tip radius, r, and the secondary dendrite arm spacing, λ_2, the average radius of the grain being denoted R and the grain density n. Note that the schematized volume for direct microscopic modeling is still oversized so as to be accessible in the representation.

Fig. 1. Schéma de (contours pointillés noirs et blancs) un domaine représentatif pour l'étude des structures dendritiques et de leurs ségrégations chimiques associées formées lors de la solidification et (contours colorés pleins) des volumes d'intégration typiques pour les équations de conservation pour (a) la modélisation microscopique directe, (b) la modélisation macroscopique directe et (c) la modélisation macroscopique indirecte. L'illustration insérée entre (a) et (b) présente une meilleure vue des volumes d'intégration et la définition du rayon de la pointe d'une dendrite, r, et de l'espacement dendritique secondaire, λ_2, le rayon moyen du grain étant noté R. A noter que le volume schématisé pour la modélisation microscopique directe est surdimensionné afin d'être accessible dans la représentation.

an extension of macroscopic modeling of solidification based on simple solidification path provided by thermodynamic considerations [40,41]. Nowadays, this indirect modeling approach is part of classical textbook on solidification [42].

Direct macroscopic modeling of structures and segregations is the last approach proposed [43–53]. It combines a direct description of the development of the grain envelopes, while its inner microstructure is simplified using indirect microscopic models. This is again illustrated by the text added in Fig. 1(b) that lists the input length scales. One of the main advantages is the possibility to take into account realistic grain envelopes. As a consequence, features such as intergranular segregations can be made available, for both columnar and equiaxed grain structures and together with columnar-to-equiaxed transitions. These models are sufficiently advanced to provide direct applications to industrial processes. However, simulations are still limited to small volumes such as those found in investment casting.

The present contribution focuses on indirect and direct macroscopic modeling of structures and segregations, thus corresponding to the description of the approaches schematized in Figs. 1(b) and 1(c). Direct microscopic modeling schematized in Fig. 1(a) is voluntary omitted because it does not permit application to real castings.

2. Indirect macroscopic modeling

Average conservation equations are first presented considering a mixture of one solid phase, s, plus one liquid phase, l. No other phase being present, the sum of their volume fraction is equal to unity: $g^{\mathrm{s}} + g^{\mathrm{l}} = 1$. Furthermore, equal and constant densities in the phases are assumed, $\rho^{\mathrm{s}} = \rho^{\mathrm{l}} = \rho_0$ together with a fixed solid phase, $\mathbf{v}^{\mathrm{s}} = 0$. As a consequence, the total mass conservation simply writes $\nabla \cdot \langle \mathbf{v} \rangle = 0$ where the average macroscopic flow velocity reduces to $\langle \mathbf{v} \rangle = g^{\mathrm{l}} \langle \mathbf{v}^{\mathrm{l}} \rangle^{\mathrm{l}}$, $\langle \mathbf{v}^{\mathrm{l}} \rangle^{\mathrm{l}}$ being the average intrinsic velocity of the liquid phase. The average momentum conservation writes [42]:

$$\rho_0 \frac{\partial \langle \mathbf{v} \rangle}{\partial t} + \frac{\rho_0}{g^{\mathrm{l}}} \left(\langle \mathbf{v} \rangle \langle \mathbf{v} \rangle \right) = \nabla \cdot \left(\mu \nabla \langle \mathbf{v} \rangle \right) - g^{\mathrm{l}} \nabla p + g^{\mathrm{l}} \rho \mathbf{g} - \frac{\mu}{K} g^{\mathrm{l}} \langle \mathbf{v} \rangle \tag{1}$$

where μ is the dynamic viscosity, p is the pressure in the liquid, $\mathbf{g}$ is the gravity vector, K is the permeability and t is the time. The permeability is calculated thanks to the Carman–Kozeny relationship considering an isotropic mushy zone domain, $K = [g^{\mathrm{l}^3} \lambda_2^2]/[180(1 - g^{\mathrm{l}})^2]$. The Boussinesq approximation is introduced to compute the fluid flow. The liquid density is thus kept constant in all terms of the momentum equation except for the gravity term where it is replaced by a function of the local solute composition in the liquid phase, $\langle w^{\mathrm{l}} \rangle^{\mathrm{l}}$, and the local temperature, T, i.e. $\rho = \rho_0[1 - \beta_{\mathrm{T}}(T - T_{\mathrm{L}}) - \beta_{\mathrm{w}}(\langle w^{\mathrm{l}} \rangle^{\mathrm{l}} - w_0)]$ where β_{T} and β_{w} denote the thermal and solutal expansion coefficients, respectively. References used to define the variations of the liquid density with the local solute composition in the liquid phase and the local temperature are the liquidus temperature of the alloy, T_{L}, and its nominal composition, w_0, respectively.

The average heat flow equation writes:

$$\rho_0 \left(\frac{\partial \langle H \rangle}{\partial t} + \langle \mathbf{v} \rangle \cdot \nabla \left\langle H^{\mathrm{l}} \right\rangle^{\mathrm{l}} \right) - \nabla \cdot \left(\langle \kappa \rangle \nabla T \right) = 0 \tag{2}$$

where $\langle H \rangle$ is the average enthalpy per unit mass and $\langle H^{\mathrm{l}} \rangle^{\mathrm{l}}$ is the average enthalpy of the liquid phase per unit mass. With the assumption of constant and equal values of the specific heat for the liquid and solid phases, $C_{\mathrm{p}}^{\mathrm{s}} = C_{\mathrm{p}}^{\mathrm{l}} = C_{\mathrm{p}}$, one can write: $\langle H \rangle = C_{\mathrm{p}}[T - T_{\mathrm{ref.}}] + g^{\mathrm{l}} \Delta_{\mathrm{s}}^{\mathrm{l}} H_{\mathrm{f}}$ and $\langle H^{\mathrm{l}} \rangle^{\mathrm{l}} = C_{\mathrm{p}}[T - T_{\mathrm{ref.}}] + \Delta_{\mathrm{s}}^{\mathrm{l}} H_{\mathrm{f}}$, where $\Delta_{\mathrm{s}}^{\mathrm{l}} H_{\mathrm{f}}$ denotes the latent heat of fusion per unit mass and $T_{\mathrm{ref.}}$ is a reference temperature. An average thermal conductivity, $\langle \kappa \rangle$, is also considered.

The average conservation of the solute mass for a binary alloy can be written:

$$\frac{\partial \langle w \rangle}{\partial t} + \langle \mathbf{v} \rangle \cdot \nabla \left\langle w^{\mathrm{l}} \right\rangle^{\mathrm{l}} - \nabla \cdot \left(D^{\mathrm{l}} g^{\mathrm{l}} \nabla \left\langle w^{\mathrm{l}} \right\rangle^{\mathrm{l}} \right) = 0 \tag{3}$$

where $\langle w \rangle$ is the average composition of solute and $\langle w^{\mathrm{l}} \rangle^{\mathrm{l}}$ is the average composition of solute in the liquid phase. D^{l} is the diffusion coefficient of the solute element in the liquid phase. Diffusion in the solid phase is neglected in comparison with that in the liquid when solving the conservation of the solute mass at the casting scale.

The main guidelines to solve Eqs. (1) to (3) in a two-dimensional representation with the finite element (FE) method are provided in Ref. [54]. A combination of the momentum conservation and the total mass conservation offers a set of equations to solve simultaneously the pressure and the average velocity fields. The average enthalpy, $\langle H \rangle$, is taken as the primary unknown in the heat flow equation. The temperature in this equation is eliminated by a first order of Taylor's expansion as a function of the average enthalpy. The primary unknown considered in the solute conservation equation is the average composition of solute, $\langle w \rangle$. The average liquid composition is eliminated by introducing a split operator technique with an Euler backward scheme, i.e. $\langle w^{\mathrm{l}} \rangle^{\mathrm{l}}$ is estimated using the value deduced from the previous time step [55]. Finally, a microsegregation model is needed to convert the average composition of solute, $\langle w \rangle$, and the average enthalpy, $\langle H \rangle$, into a temperature, T, and a fraction of solid, g^{s}. It constitutes a crucial brick for handling structure formation and will thus be further detailed later on in this contribution.

In order to provide a simple illustration of indirect macroscopic modeling, a simulation has been performed considering directional solidification of an Al–7 wt% Si alloy in a Bridgman furnace. The main alloy properties and numerical parameters are listed in the top part of Table 1. Two domains are considered. The central domain consists of a vertical rod made of the alloy with radius 4 mm and length 111 mm. It is inserted into a crucible tube closed at its bottom to hold the alloy.

Table 1
Alloy properties and numerical parameters for simulations presented in Figs. 2 and 3. The second part of the table contents the additional data required for direct macroscopic modeling.

Tableau 1
Propriétés de l'alliage et paramètres numériques pour les simulations présentées aux Figs. 2 and 3. La seconde partie du tableau contient les données additionnelles requises pour la modélisation macroscopique directe.

	Symbol	Unit	Value
Thermal conductivity	κ	$[\mathrm{W\,m^{-1}\,{}^\circ C^{-1}}]$	100.0
Heat capacity	C_p	$[\mathrm{J\,m^{-3}\,{}^\circ C^{-1}}]$	2.57×10^6
Enthalpy of fusion	$\Delta^\mathrm{l}_\mathrm{s}H_\mathrm{f}$	$[\mathrm{J\,m^{-3}}]$	9.5×10^8
Viscosity	μ	[Pa s]	10^{-3}
Thermal expansion coefficient	β_T	$[{}^\circ\mathrm{C}^{-1}]$	-1.2×10^{-4}
Solutal expansion coefficient	β_w	$[\mathrm{wt\,\%^{-1}}]$	1.4×10^{-3}
Nominal composition	w_0	[wt%]	7.0
Liquidus temperature	T_L	[°C]	618.0
Segregation coefficient	k	[–]	0.13
Eutectic composition	w_E	[wt%]	13.31
Liquidus slope	m_L	$[\mathrm{wt\,\%\,{}^\circ C^{-1}}]$	−6.5
Eutectic temperature	T_E	[°C]	577.0
Diffusion of Cu in liquid Al	D^l	$[\mathrm{m^2\,s^{-1}}]$	6.45×10^{-9}
Secondary dendrite arm spacing	λ_2	[µm]	100.0
FE mesh size	minimum	[µm]	90.0
	maximum	[µm]	900.0
Diffusion of Cu in solid Al	D^s	$[\mathrm{m^2\,s^{-1}}]$	10^{-12}
Primary dendrite arm spacing	λ_1	[µm]	1000.0
Gibbs–Thomson coefficient	Γ	[K m]	1.96×10^{-7}
Gaussian nucleation law	mean	[K]	5.0
	deviation	[K]	0.5
	saturation	$[\mathrm{m^{-3}}]$	10^{11}
Cell size		[µm]	30.0

Axisymmetrical coordinates are used. The axis of symmetry coincides with the central longitudinal axis of the two domains. Dirichlet conditions are applied at the outer boundary of the crucible to simulate Bridgman cooling. This means that space and time evolution of the temperature is chosen and imposed at the surface of the crucible so as to keep a gradient from bottom to top while cooling the entire domain at a selected cooling rate. Note that the present ratio of the cooling rate to the temperature gradient is nothing but the average velocity of the isotherms. Fig. 2(a) presents maps for (a2) the liquid velocity field, (a3) the temperature, (a4) the fraction of solid and (a5) the average solute composition at a given time. Only the alloy domain is shown. The temperature gradient is accessible through Fig. 2(a3). The almost horizontal black lines correspond to isotherms separated by only 1 °C. With a visualized height of only 10 mm, the temperature gradient is of the order of $10^3\,{}^\circ\mathrm{C\,m^{-1}}$. The imposed cooling rate at the boundary of the crucible and the heat transfer coefficient applied between the two domains lead to a vertical upward isotherm velocity equal to $50\,\mu\mathrm{m\,s^{-1}}$. It is evident from Fig. 2(a2) that movement of the liquid phase takes place with a single circulation loop that exhibits an ascending flow at the central longitudinal axis of the rod and a descending flow close to the rod periphery. A larger view actually shows that this loop occupies the entire liquid zone. Figs. 2(a3) and 2(a4) show that the isofraction of liquid departs from unity towards the top of the domain when the temperature decreases below the liquidus of the alloy, $T_\mathrm{L} = 618\,{}^\circ\mathrm{C}$. A decrease of the isofraction of liquid by only 0.05 is sufficient to almost completely stop the circulation of the liquid. The flow is mainly dictated by the small radial component of the temperature gradient. The small lateral heat flow between the crucible and the alloy is thus sufficient to generate the slightly curved isotherms shown in Fig. 2(a3) and induced the fluid flow observed in Fig. 2(a2). The fluid flow is yet not sufficient to create significant macrosegregation, since the composition is found to vary within less than 0.2 wt% around the nominal composition in Fig. 2(a5).

3. From indirect to direct macroscopic modeling

For the simulation in Fig. 2(a), the simplest possible microsegregation model has been considered based on local thermodynamic equilibrium with uniform compositions in both the solid and the liquid phases. In the case of a closed system, such approximation would be named inverse lever rule. However, this approximation is known to be inappropriate for most metallic alloys. Not only diffusion in the solid is limited, but diffusion in the liquid phase also controls the formation of the structure and creates zones of undercooled liquid. The later reasons justify the development of structural models based on length scales to compute diffusion in phases and mass exchanges at the solid–liquid interface. For instance, in the case of an idealized equiaxed dendrite nucleated in an undercooled liquid, one can use a spherical grain envelope with a radius given by the position of its dendrite tips. Because good approximations of the growth kinetics of the dendrite tip of radius r are also known thanks to indirect microscopic models developed over the last 30 years [3], the time integration of such an envelope is directly performed to compute the grain radius, R [42]. A dendrite arm spacing, λ_2, is then used to describe the inner microstructure of the grain. Thus, with only a few length scale parameters, and assuming a final grain size inversely

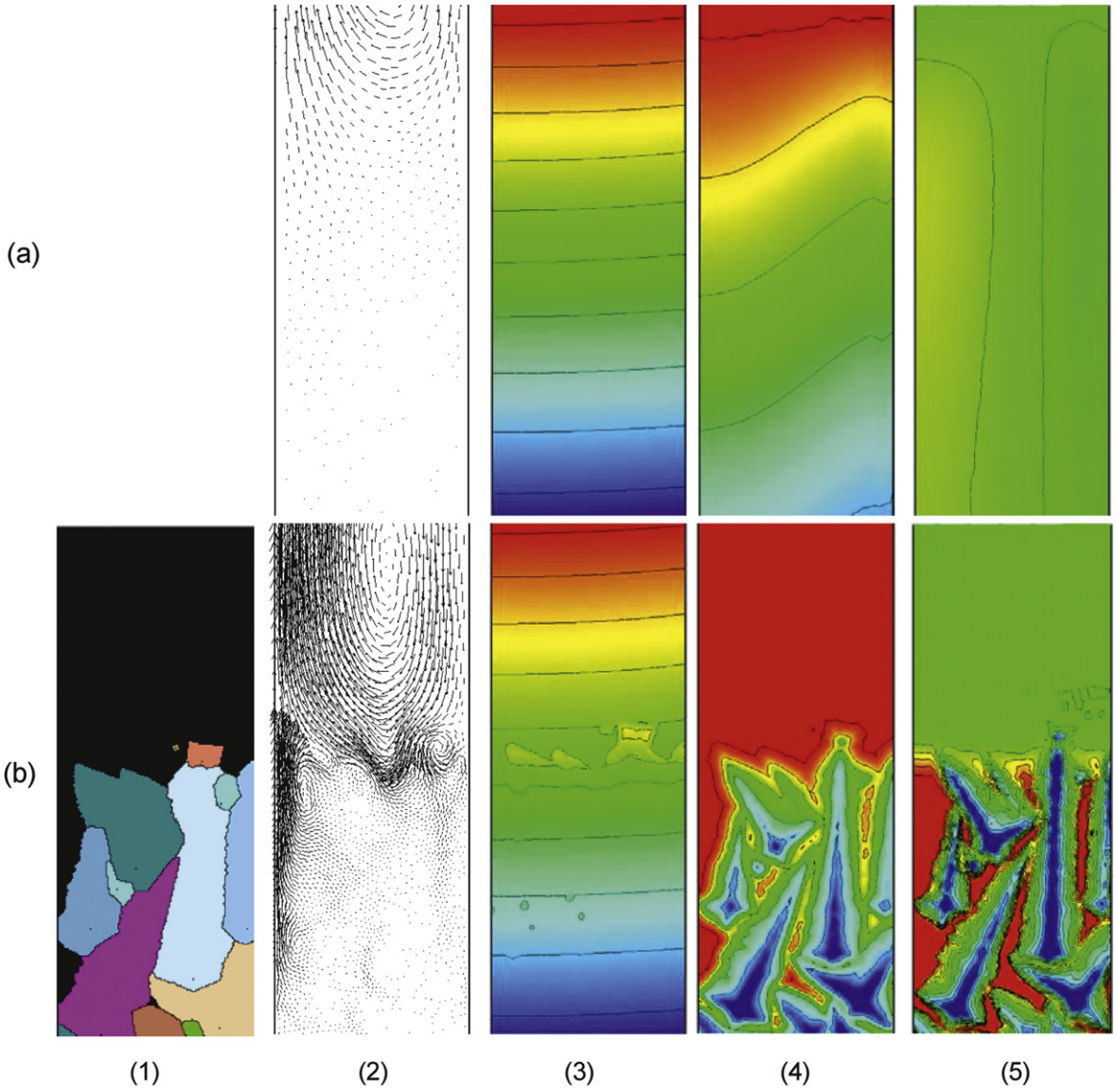

Fig. 2. Simulation snapshots of the directional solidification of an Al–7 wt% Si rod in a Bridgman furnace using (a) indirect macroscopic modeling and (b) direct macroscopic modeling. The columns display (1) the growing grain envelopes computed by direct macroscopic modeling, which are not predicted by indirect macroscopic modeling, (2) the velocity of the liquid flow, (3) the temperature map below the liquidus temperature $T_L = 618\,^{\circ}\mathrm{C}$, T [blue: 608 °C, red: 618 °C, interval between contours: 1 °C], (4) fraction of liquid, g^l [blue: 0.75, red: 1, interval between contours: 0.05], and (5) the average composition of Si around the nominal composition $\langle w_{Si}\rangle = 7$ wt%, [blue: 6.5 wt%, red: 7.5 wt%, interval between contours: 0.1 wt%]. Pulling velocity of the Bridgman furnace: 50 $\mu m\,s^{-1}$, vertical axis of symmetry located at the left-hand side of the figures corresponding to the longitudinal central axis of the rod, rod diameter: 4 mm, rod length: 111 mm (field of view is only 10 mm height), macroscopic modeling using the finite element method (b) coupled with a cellular automaton method for the description of the grain envelopes.

Fig. 2. Instantanés simulés de la solidification dirigée d'un cylindre d'Al–7 %pds Si dans un four Bridgman avec (a) une modélisation macroscopique indirecte et (b) une modélisation macroscopique directe. Les colonnes montrent (1) les enveloppes des grains en croissance calculées par la modélisation macroscopique directe, qui ne sont pas prédites par la modélisation macroscopique indirecte, (2) la vitesse d'écoulement du liquide, (3) la carte de température sous la température du liquidus $T_L = 618\,^{\circ}\mathrm{C}$, T [bleue : 608 °C, rouge : 618 °C, intervalle entre les contours : 1 °C], (4) la fraction de liquide, g^l [bleue : 0.75, rouge : 1, intervalle entre les contours : 0.05], et (5) la composition moyenne du Si autour de la composition nominale $\langle w_{Si}\rangle = 7$ %pds, [bleue : 6.5 %pds, rouge : 7.5 %pds, intervalle entre les contours : 0.1 %pds]. Vitesse de tirage du four Bridgman : 50 $\mu m\,s^{-1}$, axe de symétrie vertical situé à gauche des figures et correspondant à l'axe longitudinal central du barreau, modélisation macroscopique utilisant la méthode des éléments finis (b) couplée à la méthode des automates cellulaires pour la description des enveloppes de grain.

proportional to the third-power of the final grain density, n, one can build a model where mass exchange is described in the solid phase, in the interdendritic liquid, but also in the extradendritic liquid. This was first done for binary alloys and a single solid phase [18–22]. Current extensions consider multicomponent alloys [23–25] and formation of several solid phases [26,27]. Implementation of these microsegregation analyses for a single grain has then been carried out for application to

cast parts [28] with the possibility to account for the transport of equiaxed grains in the liquid, macrosegregation, as well as for transitions between columnar and equiaxed grains [29–38]. This coupling between grain structure-base microsegregation models and macroscopic analyses of heat and mass transports is still mainly two-dimensional and has not yet been coupled with thermomechanical analyses. The later limitation will need to be released if one wishes to fully describe the important interplays between the thermomechanical deformations of the solid phases and the macrosegregation while accounting for the pertinent microscopic length scales of the structure.

The main difference between indirect and direct modeling of structures and segregation taking place upon solidification is the topological tracking of the envelope of the grains. For that purpose, several methods have been proposed based on mesoscopic phase field method [51] or front tracking methods of the mushy zone–liquid boundary [52,53]. The cellular automaton (CA) method is used in the present contribution. Its bases for the modeling of nucleation and growth of the grain envelopes are not given into details and can be found elsewhere [47]. Instead, the next section focuses on the coupling of the CA method with the FE solution of Eqs. (1) to (3). The interest of this presentation lies in the fact that an indirect microsegregation model initially derived for indirect macroscopic modeling [19,20] is now used hereafter in order to locally compute the solidification of each CA cell, i.e. as part of direct macroscopic modeling of the grain envelopes. Thus, while direct representation of the grain envelopes is implemented in direct macroscopic modeling, tracking of the solid–liquid phase interface can be avoided. This strategy of local microsegregation analyses is at the heart of the recent developments of the coupled CAFE model [46–50].

4. Direct macroscopic modeling

The alloy domain initially divided into an FE mesh using triangles F defined by nodes n_i^F $(i = [1, 3])$ is further divided into a regular lattice of fine squares named CA cells. Each cell v is defined by its center coordinates, C_v, and is located in a given element F. Linear interpolation coefficients are defined between a node n_i^F $(i = [1, 3])$ and the cell v. A variable defined at the FE nodes can thus be interpolated at a given CA cell. Similarly, information computed onto the CA grid can be summed up and projected onto the FE mesh. Each cell v is also attributed with an index, I_v, that defines its state. At the beginning of a simulation starting from a superheated melt, all cells v are in the liquid state, i.e. $I_v = 0$. As nucleation and growth proceed, the index of cell v is changed to a non-zero value, i.e. $I_v \neq 0$. The growth of the structure in cell v is also characterized by the size of its local mushy zone defined by the extension of four $\langle 10\rangle$ directions, $R_v^{\langle 10\rangle}$, that represent the dendrite trunks and arms. The cell is then in a mushy state, i.e. made of a mixture of the solid and liquid phases. Its fraction of phases then needs to be determined. This is again the role of the local microsegregation model presented hereafter.

The liquid phase is subdivided into a uniform composition interdendritic liquid, d, plus an extradendritic liquid, l, as initially proposed by Rappaz and Thévoz [18]. With the solid phase, a total of three "phases" is thus considered for mass balances. A mushy zone volume fraction assigned to each cell v, g_v^{m}, is defined as the volume fraction of the solid phase s, g_v^{s}, plus the interdendritic liquid phase d, g_v^{d}: $g_v^{\mathrm{m}} = g_v^{\mathrm{s}} + g_v^{\mathrm{d}}$. It is estimated by an average of the lengths that define the size of the growing shape associated to cell v, $R_v^{\langle 10\rangle}$, as $g_v^{\mathrm{m}} = (1/4)\sum_{\langle 10\rangle}(R_v^{\langle 10\rangle}/R_v^{\mathrm{f}})^2$. The final radius associated to cell v, R_v^{f}, is defined by the spatial limit for the growth of the equilateral quadrangle, which is of the order of several secondary arm spacings, typically of the order of the primary arm. In the case of a dendritic structure, this limit is chosen proportional to the primary dendrite arm spacing, $R_v^{\mathrm{f}} = \lambda_1/2$. The conversion of the interpolated enthalpy, $\langle H_v\rangle$, and average composition, $\langle w_v\rangle$, at each CA cell v is first carried out to compute the temperature, T_v, and fraction of solid, g_v^{s}. The fields at the CA cells are finally projected back to the FE nodes [46,47]. Assuming equal and constant densities in all phases, one can write: $g_v^{\mathrm{s}} + g_v^{\mathrm{d}} + g_v^{\mathrm{l}} = 1$ and $\langle w_v\rangle = g_v^{\mathrm{s}}\langle w_v^{\mathrm{s}}\rangle^{\mathrm{s}} + g_v^{\mathrm{d}}\langle w_v^{\mathrm{d}}\rangle^{\mathrm{d}} + g_v^{\mathrm{l}}\langle w_v^{\mathrm{l}}\rangle^{\mathrm{l}}$. A segregation model is required to model the time evolution of the average volume fraction and composition of the solid phase s, $g_v^{\mathrm{s}}\langle w_v^{\mathrm{s}}\rangle^{\mathrm{s}}$, the interdendritic liquid phase d, $g_v^{\mathrm{d}}\langle w_v^{\mathrm{d}}\rangle^{d}$, and the extradendritic liquid phase l, $g_v^{\mathrm{l}}\langle w_v^{\mathrm{l}}\rangle^{\mathrm{l}}$. This is done using the following solute mass balance in the three phases present in each cell v [19,20]:

$$\frac{\partial}{\partial t}\left(g_v^{\mathrm{s}}\left\langle w_v^{\mathrm{s}}\right\rangle^{\mathrm{s}}\right) = w_v^{\mathrm{sd}} S_v^{\mathrm{sd}} v_v^{\mathrm{sd}} + S_v^{\mathrm{sd}}\frac{D^{\mathrm{s}}}{l_v^{\mathrm{sd}}}\left(w_v^{\mathrm{sd}} - \left\langle w^{\mathrm{s}}\right\rangle_v^{\mathrm{s}}\right) \tag{4}$$

$$\frac{\partial}{\partial t}\left(g_v^{\mathrm{d}}\left\langle w_v^{\mathrm{d}}\right\rangle^{\mathrm{d}}\right) = -w_v^{\mathrm{sd}} S_v^{\mathrm{sd}} v_v^{\mathrm{sd}} - w_v^{\mathrm{ld}} S_v^{\mathrm{ld}} v_v^{\mathrm{ld}} - S_v^{\mathrm{sd}}\frac{D^{\mathrm{s}}}{l_v^{\mathrm{sd}}}\left(w_v^{\mathrm{sd}} - \left\langle w^{\mathrm{s}}\right\rangle_v^{\mathrm{s}}\right) - S_v^{\mathrm{ld}}\frac{D^{\mathrm{l}}}{l_v^{\mathrm{ld}}}\left(w_v^{\mathrm{ld}} - \left\langle w^{\mathrm{l}}\right\rangle_v^{\mathrm{l}}\right) + g_v^{\mathrm{d}}\dot{\varphi}_v^{\mathrm{d}} \tag{5}$$

$$\frac{\partial}{\partial t}\left(g_v^{\mathrm{l}}\left\langle w_v^{\mathrm{l}}\right\rangle^{\mathrm{l}}\right) = w_v^{\mathrm{ld}} S_v^{\mathrm{ld}} v_v^{\mathrm{ld}} + S_v^{\mathrm{ld}}\frac{D^{\mathrm{l}}}{l_v^{\mathrm{ld}}}\left(w_v^{\mathrm{ld}} - \left\langle w^{\mathrm{l}}\right\rangle_v^{\mathrm{l}}\right) + g_v^{\mathrm{l}}\dot{\varphi}_v^{\mathrm{l}} \tag{6}$$

where w_v^{sd} is the average composition of the solid phase at the s/d interface and w_v^{ld} is the average composition of the liquid phase at the l/d interface. Mass exchanges are considered between the solid phase and the interdendritic liquid phase through the interfacial area concentration, S_v^{sd}, as well as between the extradendritic liquid phase and the interdendritic liquid phase through the interfacial area concentration, S_v^{ld}, while the mass exchange between the solid phase and the extradendritic liquid phase is neglected. Solute profiles are assumed in the solid phase from the solid–interdendritic liquid interface, l_v^{sd}, and in the extradendritic liquid phase from the interdendritic liquid–extradendritic liquid boundary, l_v^{ld}. The expressions for the interfacial area concentrations and the diffusion lengths are provided in Ref. [49]. Complete mixing of the interdendritic liquid composition and continuity of the composition at interface l/d are assumed, $w_v^{\mathrm{ld}} = \langle w_v^{\mathrm{d}}\rangle^{\mathrm{d}}$, together

with equilibrium at the s/d interface. Thus, at temperature T, readings of the liquidus and solidus curves of the equilibrium phase diagram respectively give $\langle w_v^{\mathrm{d}}\rangle^{\mathrm{d}}$ and w_v^{sd}. With the partition ratio k, one also has $w_v^{\mathrm{sd}} = k\langle w_v^{\mathrm{d}}\rangle^{\mathrm{d}}$.

The time derivative of the volume fraction of the solid phase, $\partial g_v^{\mathrm{s}}/\partial t$, can be written as a function of its interfacial area concentration, S_v^{sd}, and the normal velocity of the s/d interface, v_v^{sd}, as $S_v^{\mathrm{sd}} v_v^{\mathrm{sd}} = \partial g_v^{\mathrm{s}}/\partial t = -\partial g_v^{\mathrm{d}}/\partial t$. Similarly one can write $S_v^{\mathrm{ld}} v_v^{\mathrm{ld}} = \partial g_v^{\mathrm{l}}/\partial t = -\partial g_v^{m}/\partial t$. The volume fraction of the interdendritic liquid phase and the external liquid phase are respectively defined and computed as $g_v^{\mathrm{d}} = g_v^{\mathrm{m}} - g_v^{\mathrm{s}}$ and $g_v^{\mathrm{l}} = 1 - g_v^{\mathrm{m}}$. The growth rate of the mushy zone is calculated with a dendrite tip growth kinetics model, $v_v^{\mathrm{ld}} = v_v^{\langle 10\rangle}$ [56]:

$$v_v^{\langle 10\rangle} = \frac{\partial R_v^{\langle 10\rangle}}{\partial t} = \frac{4\sigma^* D^{\mathrm{l}} m_{\mathrm{L}}(k-1) w_v^{\mathrm{ls}}}{\Gamma}\left(\mathrm{Iv}^{-1}(\Omega_v)\right)^2 \tag{7}$$

$$\Omega_v = \frac{w_v^{\mathrm{ls}} - \langle w_v\rangle}{w_v^{\mathrm{ls}}(1-k)} \tag{8}$$

where Γ is the Gibbs–Thomson coefficient, Iv^{-1} is the inverse of the Ivantsov function [3], σ^* is a stability constant taken equal to $1/(4\pi^2)$, m_{L} is the liquidus slope of the phase diagram. The local supersaturation, Ω_v, is defined at the tip of the growing dendrites located at the growth front, i.e. between the mushy zone and the extradendritic liquid. It is expressed as a function of a boundary layer correlation [56]. The curvature undercooling is taken into account by adding its contribution to the solutal undercooling and assuming local equilibrium at the dendrite tip for the calculation of the liquid composition w_v^{ls}.

The source terms in Eqs. (5) and (6), $\dot\varphi_v^{\mathrm{d}}$ and $\dot\varphi_v^{\mathrm{l}}$, account for the solute mass exchange of the cell v with its surrounding. By summing up $g_v^{\mathrm{d}}\dot\varphi_v^{\mathrm{d}}$ and $g_v^{\mathrm{l}}\dot\varphi_v^{\mathrm{l}}$, we obtain the equivalent terms at the scale of the CA model of the solute diffusion term, $\nabla\cdot(g^{\mathrm{f}} D^{\mathrm{l}}\nabla\langle w^{\mathrm{f}}\rangle^{\mathrm{f}})$, computed by the FE model and interpolated at cell v. The relative portions, $\dot\varphi_v^{\mathrm{l}}$ and $\dot\varphi_v^{\mathrm{d}}$, can be quantified by introducing a partition ratio for diffusion in the liquid, $\varepsilon_{\mathrm{D}^{\mathrm{l}}} = \dot\varphi_v^{\mathrm{l}}/\dot\varphi_v^{\mathrm{d}}$. The following correlation is proposed as a function of the volume fraction of the interdendritic liquid phase and the extradendritic liquid phase: $\varepsilon_{\mathrm{D}^{\mathrm{l}}} = g_v^{\mathrm{l}}/(g_v^{\mathrm{l}} + g_v^{\mathrm{d}})$. Hence, terms $g_v^{\mathrm{d}}\dot\varphi_v^{\mathrm{d}}$ and $g_v^{\mathrm{l}}\dot\varphi_v^{\mathrm{l}}$ can be evaluated from the solution of Eq. (3). Finally, with Eqs. (4)–(8) and a local heat balance for cell v, $\partial\langle H_v\rangle/\partial t = c_{\mathrm{p}}\partial T_v/\partial t - \Delta_{\mathrm{s}}^{\mathrm{l}} H_{\mathrm{f}}\partial g_v^{\mathrm{s}}/\partial t$, a complete system of differential equations is obtained. A splitting scheme is applied to the differential equations, together with a first-order Taylor series. An iterative algorithm is implemented to calculate the solution. More details are available in Ref. [49]. Once the prescribed growth temperature of the eutectic structure is reached, a simple isothermal transformation is assumed in order to transform the remaining liquid phase, $g_v^{\mathrm{d}} + g_v^{\mathrm{l}}$, into a volume fraction of eutectic, g_v^{E}. During the formation of the eutectic, no temperature variation over time is assumed up to full solidification [47,53].

Fig. 2(b) shows the result of a simulation with the same materials and boundary conditions as for Fig. 2(a) but using the direct macroscopic model. The alloy properties and parameters are listed in Table 1. The additional illustration (b1) shows the grain envelopes at the time of the snapshot, which were not predicted by indirect modeling. In fact, the position of the grain envelopes corresponds to the location where the mushy zone is present. This is clearly seen when considering Fig. 2(b4). It is indeed found that the contour of the isofraction of liquid equal to 1 coincides with the position of the grain envelope in Fig. 2(b1). By extrapolation, one could have composed a single grain envelope as Fig. 2(a1), choosing to implicitly select its position by the isofraction of liquid equal to 1 in Fig. 2(a4). Note that this isofraction does not exactly superimpose to the liquidus of the alloy shown in Fig. 2(a3). This is due to macrosegregation. Indeed, perturbation of the solute composition does vary the local liquidus temperature. The temperature maps in Figs. 2(a3) and 2(b3) are very comparable since the cooling of the whole sample is driven by the Bridgman configuration imposed on the crucible walls. However, perturbation occurs close to the growing envelopes in Fig. 2(b3). The effect is due to the latent heat released upon nucleation and growth. The kinetics of solidification is much higher than in the rest of the mushy zone during the development of the grain envelopes into the undercooled liquid. This is clear when considering the distance between isofractions of liquid in Fig. 2(b4) compared to 2(a4). Such effect is well known and leads to the recalescence observed in situation of low temperature gradient and cooling rate. In the present simulation, it remains very limited and the prediction of its magnitude may be discussed due to the two-dimensional axisymmetrical approximation. A main circulation loop is predicted in Fig. 2(b2). The flow is yet found to vary more abruptly when approaching the grain envelopes. Again, this is due to the faster solidification kinetics in the periphery of the growth fronts. Note that the convection loop extends easily in the undercooled liquid, i.e. about 4 mm lower that in indirect modeling. Also of interest are the small recirculation loops just ahead of the grain envelopes, i.e. in the liquid located in between the grain envelopes. The average composition of Si is presented in Fig. 2(b5). This map is certainly the most interesting result to compare with indirect modeling. Together with Fig. 2(b1), it shows that a strong accumulation of Si takes place at the grain boundaries. Fig. 2(b4) also shows how the highest Si content delays solidification at the grain boundaries. Thus, upon further cooling, the fraction of liquid remaining when reaching the eutectic temperature is different in intragranular and intergranular regions. The expected consequence is shown in Fig. 3(a2), revealing inhomogeneous distribution of the fraction of eutectic and the final grain structure in the same zone as in Fig. 2(b). In fact, because macrosegregation is mainly dictated here by the transport of the species by convection, the difference of the liquid flow between indirect and direct modeling and the preferred recirculation at grain boundaries in Fig. 2(b2) explain the intergranular patterns in Figs. 2(b4) and 2(b5).

In order to study the effect of the pulling velocity of the Bridgman furnace on structure and segregation, the Dirichlet boundary conditions have been modified. An increase of the cooling rate is considered while keeping approximately constant

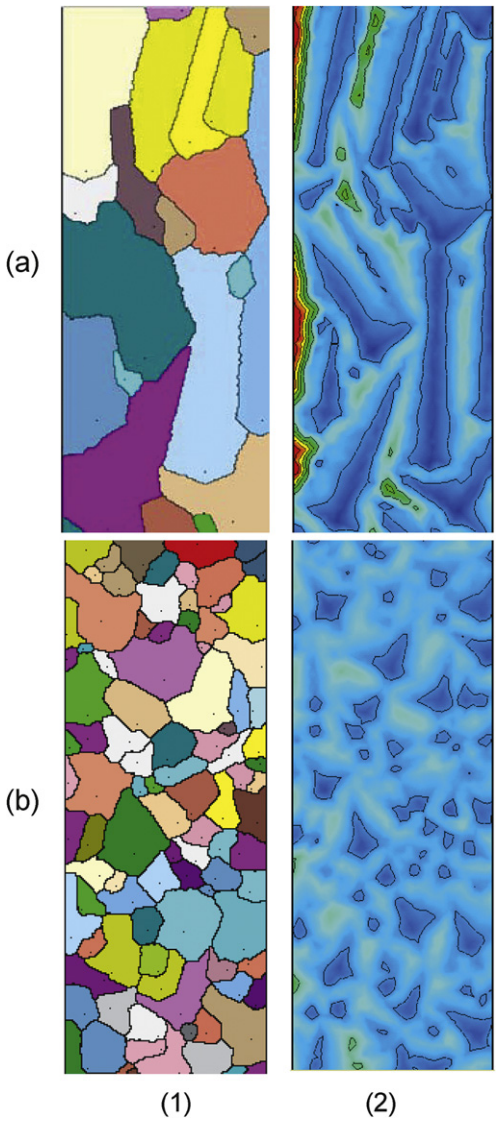

Fig. 3. Final distributions of (1) the grain structure and (2) the fraction of eutectic, g^{E} [blue: 0.35, red: 0.95, interval between contours: 0.05], computed using direct macroscopic modeling for two pulling velocities of the Bridgman furnace: (a) 50 $\mu m\,s^{-1}$ (same as for Fig. 2) and (b) 150 $\mu m\,s^{-1}$. Vertical axis of symmetry located at the left-hand side of the figures corresponding to the longitudinal central axis of the rod, macroscopic modeling using the finite element method coupled with a cellular automaton method for the description of the grain envelopes.

Fig. 3. Distributions finales de (1) la structure de grains et (2) la fraction d'eutectique, g^{E} [bleue : 0.35, rouge : 0.95, intervalle entre contours : 0.05], calculée par modélisation macroscopique directe pour deux vitesses de tirage du four Bridgman : (a) 50 $\mu m\,s^{-1}$ (même que pour la Fig. 2) et (b) 150 $\mu m\,s^{-1}$. Axe de symétrie vertical situé à gauche des figures et correspondant à l'axe longitudinal central du barreau, modélisation macroscopique utilisant la méthode des éléments finis couplée à la méthode des automates cellulaires pour la description des enveloppes de grain.

the overall temperature gradient. The isotherm velocity does then reach 150 $\mu m\,s^{-1}$ in Fig. 3(b). The result shows an increase of the grain density accompanied by a decrease of the intergranular fraction of eutectic. Such prediction of segregation and fraction of phases formed upon solidification is not common in the literature. Intergranular segregation is at the origin of several technologically important phenomena. One could mention hot tearing as a classical defect heavily linked to the presence of liquid films at intergranular regions. The definition of homogenization heat treatment of cast parts to suppress or reduce the presence of undesired phases is another example. The latter phenomena have clearly been identified as dependent on the grain density. Thus, the present direct macroscopic model of structures and segregations is able to tackle these issues.

5. Conclusions

Direct macroscopic modeling of structures and segregations has been presented using a finite element (FE) method coupled with a cellular automaton (CA) method. The CA is used to directly track the nucleation and growth of individual grain

envelopes. While modeling of microsegregation is still indirect and requires typical average length scales of the microstructure, the main advantage of the CAFE model is the possibility to reach prediction of segregation at the scale of the cast part with account of the variations induced by the grain structure. This is not the case when considering direct microscopic modeling of the microstructure.

Direct macroscopic modeling also shows the difference between intragranular and intergranular segregations. This result is believed to be of prime importance for the prediction of defects such as hot tearing. In case of extension to multicomponent alloys, it is also expected that not only the fraction of the phases can be predicted but also their nature, inside and at the periphery of the grains. Such developments are currently under progress.

Finally, it is important to recall that coupling with thermomechanical deformation is still not considered for the prediction of grain boundary segregation during solidification. However, each individual grain is an independent network of solid that is expected to deform differently from its neighbor. Because its deformation is linked to mass transport of liquid rich solute, it induces macrosegregation [57,58]. Direct macrostructure modeling thus needs to be extended to account for the flow of the liquid at grain boundaries due to thermomechanical deformations.

Acknowledgements

The cellular automaton–finite element model used in this contribution for direct modeling of the grain structures and segregations was funded thanks to grants from the European Space Agency (CETSOL contract 14313/01/NL/SH, NEQUISOL contract 15236/02/NL/SH).

References

[1] M. Rappaz, Int. Mater. Rev. 34 (1989) 93.
[2] T.P. Battle, Int. Mater. Rev. 37 (1992) 249.
[3] R. Trivedi, W. Kurz, Int. Mater. Rev. 39 (1994) 49.
[4] H.W. Kerr, W. Kurz, Int. Mater. Rev. 41 (1996) 129.
[5] C. Beckermann, Int. Mater. Rev. 47 (2002) 243.
[6] J.A. Spittle, Int. Mater. Rev. 51 (2006) 247.
[7] A.F. Gourgues-Lorenzon, Int. Mater. Rev. 52 (2007) 65.
[8] M. Asta, C. Beckermann, A. Karma, W. Kurz, R. Napolitano, M. Plapp, G. Purdy, M. Rappaz, R. Trivedi, Acta Mater. 57 (2009) 941.
[9] Y. Saito, G. Goldbeck-Wood, H. Müller-Krumbhaar, Phys. Rev. A 38 (1988) 2148.
[10] W.J. Boettinger, J.A. Warren, C. Beckermann, A. Karma, Annu. Rev. Mater. Res. 32 (2002) 163.
[11] I. Steinbach, Mod. Simul. Mater. Sci. Eng. 17 (2009) 1.
[12] A. Jacot, M. Rappaz, Acta Mater. 50 (2002) 1909.
[13] W. Wang, P.D. Lee, Acta Mater. 51 (2003) 2971.
[14] N. Provatas, N. Goldenfeld, J.A. Dantzig, Phys. Rev. Lett. 80 (1998) 3308.
[15] L. Tan, N. Zabaras, J. Comp. Phys. 211 (2006) 36.
[16] J.-C. Ramirez, C. Beckermann, A. Karma, H.-J. Diepers, Phys. Rev. E 69 (2004) 051607.
[17] A. Karma, W.-J. Rappel, J. Cryst. Growth 54 (1997) 174.
[18] M. Rappaz, Ph. Thévoz, Acta Metall. 35 (1987) 2929.
[19] C.Y. Wang, C. Beckermann, Metall. Trans. A 24 (1993) 2787.
[20] C.Y. Wang, C. Beckermann, Mater. Sci. Eng. A 171 (1993) 199.
[21] O. Grong, A.K. Dahle, M.I. Onsoien, L. Arnberg, Acta Mater. 46 (1998) 5045.
[22] Ø. Nielsen, B. Appolaire, H. Combeau, A. Mo, Metall. Mater. Trans. A 32 (2001) 2049.
[23] M. Rappaz, W.J. Boettinger, Acta Mater. 47 (1999) 3205.
[24] B. Appolaire, H. Combeau, G. Lesoult, Mater. Sci. Eng. A 487 (2008) 33.
[25] H. Zhang, Ch.-A. Gandin, H. Ben Hamouda, D. Tourret, K. Nakajima, J. He, ISIJ Int. 50 (2010).
[26] Ch.-A. Gandin, S. Mosbah, Th. Volkmann, D. Herlach, Acta Mater. 56 (2008) 3023.
[27] D. Tourret, Ch.-A. Gandin, Acta Mater. 57 (2009) 2066.
[28] Ph. Thévoz, M. Rappaz, J.-L. Desbiolles, in: Ch.M. Bickert (Ed.), Light Metals, TMS Publ., Warrendale, PA, USA, 1990, p. 975.
[29] C.Y. Wang, C. Beckermann, Metall. Mater. Trans. A 27 (1996) 2754.
[30] C.Y. Wang, C. Beckermann, Metall. Mater. Trans. A 27 (1996) 2765.
[31] C. Beckermann, C.Y. Wang, Metall. Mater. Trans. A 27 (1996) 2784.
[32] M.A. Martorano, C. Beckermann, Ch.-A. Gandin, Metall. Mater. Trans. A 34 (2003) 1657.
[33] A.I. Ciobanas, Y. Fautrelle, J. Phys. D: Appl. Phys. 40 (2007) 3733.
[34] A.I. Ciobanas, Y. Fautrelle, J. Phys. D: Appl. Phys. 40 (2007) 4310.
[35] M. Wu, A. Ludwig, Metall. Mater. Trans. A 38 (2007) 1465.
[36] M. Wu, A. Ludwig, Acta Mater. 57 (2009) 5621.
[37] M. Wu, A. Ludwig, Acta Mater. 57 (2009) 5631.
[38] M. Zaloznic, H. Combeau, Comp. Mater. Sci. 48 (2010) 1.
[39] M. Zaloznic, H. Combeau, Comp. Mater. Sci. 48 (2010) 11.
[40] M.C. Schneider, C. Beckermann, Metall. Mater. Trans. A 26 (1995) 2373.
[41] S. Gouttebroze, M. Bellet, H. Combeau, C. R. Mécanique 335 (2007) 269.
[42] J.A. Dantzig, M. Rappaz, Solidification, EPFL Press, Lausanne, CH, 2009.
[43] Ch.-A. Gandin, M. Rappaz, Acta Metall. 42 (1994) 2233.
[44] Ch.-A. Gandin, J.-L. Desbiolles, M. Rappaz, Ph. Thévoz, Metall. Mater. Trans. A 30 (1999) 3153.
[45] H. Takatani, Ch.-A. Gandin, M. Rappaz, Acta Mater. 48 (2000) 675.
[46] G. Guillemot, Ch.-A. Gandin, H. Combeau, ISIJ Int. 46 (2006) 880.
[47] G. Guillemot, Ch.-A. Gandin, M. Bellet, J. Cryst. Growth 303 (2007) 58.

[48] Ch.-A. Gandin, J. Blaizot, S. Mosbah, M. Bellet, G. Zimmermann, L. Sturz, D.J. Browne, S. McFadden, H. Jung, B. Billia, N. Mangelinck, H. Nguyen-Thi, Y. Fautrelle, X. Wang, Mater. Sci. Forum 649 (2010) 189.
[49] S. Mosbah, Ch.-A. Gandin, M. Bellet, Metall. Mater. Trans. A 41 (2010) 651.
[50] S. Mosbah, M. Bellet, Ch.-A. Gandin, Mater. Sci. Forum 649 (2010) 237.
[51] I. Steinbach, C. Beckermann, Acta Mater. 47 (1999) 971.
[52] D.J. Browne, ISIJ Int. 45 (2005) 37.
[53] R. Heringer, Ch.-A. Gandin, G. Lesoult, H. Henein, Acta Mater. 54 (2006) 4427.
[54] W. Liu, Finite element modelling of segregation and thermomechanical phenomena in solidification processes, Ph.D. thesis, Ecole Nationale Supérieure des Mines de Paris, Paris, France, 2005.
[55] C. Prakash, V. Voller, Numer. Heat Trans. B 15 (1989) 171.
[56] Ch.-A. Gandin, G. Guillemot, B. Appolaire, N.T. Niane, Mat. Sci. Eng. A 342 (2003) 44.
[57] G. Lesoult, Ch.-A. Gandin, N.T. Niane, Acta Mater. 51 (2003) 5263.
[58] G. Lesoult, Ch.-A. Gandin, N.T. Niane, Acta Mater. 52 (2004) 531.